Overcoming Nanoscale Inhomogeneities in Thin-film Perovskites via Exceptional Post-Annealing Grain Growth for Enhanced Photodetection

Tian Du[1,5,*,#], *Filipe Richheimer*[2], *Kyle Frohna*[3], *Nicola Gasparini*[4], *Lokeshwari Mohan*[1,5], *Ganghong Min*[4], *Weidong Xu*[4], *Thomas J. Macdonald*[4], *Haozhen Yuan*[1], *Sinclair R. Ratnasingham*[1,5], *Saif Haque*[4], *Fernando A. Castro*[2], *James R. Durrant*[4,6], *Samuel D. Stranks*[3,7], *Sebastian Wood*[2], *Martyn A. McLachlan*[5] *and Joe Briscoe*[1,*]

[1]School of Engineering and Materials Science and Materials Research Institute, Queen Mary University of London, London E1 4NS, United Kingdom.
[2]National Physical Laboratory, Hampton Road, Teddington TW11 0LW, United Kingdom.
[3]Cavendish Laboratory, JJ Thomson Avenue, Cambridge CB3 0HE, United Kingdom.
[4]Department of Chemistry and Centre for Processable Electronics, Imperial College, London, W12 0BZ, United Kingdom.
[5]Department of Materials and Centre for Processable Electronics, Imperial College, London, W12 0BZ, United Kingdom.
[6]SPECIFIC IKC, College of Engineering, Swansea University, SA2 7AX, United Kingdom.
[7]Department of Chemical Engineering & Biotechnology, University of Cambridge, Philippa Fawcett Drive, Cambridge CB3 0AS, United Kingdom.

Corresponding authors:

[*]Email: j.briscoe@qmul.ac.uk
[*]Email: t.du@qmul.ac.uk.

Abstract

Antisolvent-assisted spin coating has been widely used for fabricating metal halide perovskite films with smooth and compact morphology. However, localized nanoscale inhomogeneities exist in these films owing to rapid crystallization, undermining their overall optoelectronic performance. Here we show that by relaxing the requirement for film smoothness, outstanding film quality can be obtained simply through a post-annealing grain growth process without passivation agents. The morphological changes, driven by a vaporized methylammonium chloride (MACl)-dimethylformamide (DMF) solution, lead to comprehensive defect elimination. Our nanoscale characterization visualizes the local defective clusters in the as-deposited film and their elimination following treatment, which couples with the observation of emissive grain boundaries and excellent inter- and intra-grain optoelectronic uniformity in the polycrystalline film. Overcoming these performance-limiting inhomogeneities results in enhancement of photoresponse to low-light (< 0.1 mW cm^{-2}) illumination by up to 40-fold, yielding high-performance photodiodes with superior low-light detection.

Key words: Thin-film perovskites, nanoscale inhomogeneities, grain growth, photoresponse, photodetection.

Solution-processed metal halide perovskites (MHPs) are inherently polycrystalline, consisting of crystallographic[1] and electronic defects.[2] Although high-performance solar cells can be achieved from these solution-processed films,[3] as the trap states in MHPs are reported to be less detrimental under solar irradiance,[4] the impact of trap-mediated recombination is non-negligible at low carrier densities.[5,6] Under weak illumination, for example, trap-mediated recombination may completely switch off charge transfer to contact layers.[4,7] Hence, controlling crystallographic defects and thus electronic trap states in thin-film MHPs is of great importance to devices working under dark or low-light conditions, such as transistors,[8] photodetectors[9] or indoor solar cells.[10]

Since first introduced,[11] the "antisolvent washing" for spin coating of perovskite films has become the dominant technique used for high-performing devices. The overriding factor driving the uptake of this method is the need for smooth, compact, and planar perovskite films for subsequent deposition of charge transport layers by solution-processed routes. However, the rapid perovskite crystallization induced by antisolvent washing and subsequent thermal annealing gives rise to relatively small grains (~ 150 – 200 nm in diameter). These small grains typical demonstrate a strongly heterogeneous shape owing to limited space for post-crystallization growth. As such, local inhomogeneity exists in these films in terms of material composition,[12] crystallographic defects,[13] trap density[14] and lattice strains[15], with the local inhomogeneity being observed not only inter-grain[16,17] but also intra-grain.[18,19] In addition, the prevalent grain boundaries (GB) in polycrystalline films are heterogeneous to the grain interior in nature[20,21] and they typically host a variety of crystallographic defects.[22] Therefore, overcoming the local inhomogeneity, particularly at the GBs, is a critical route towards improvement of the overall quality of polycrystalline films.

Post-deposition crystal growth is widely used to improve the grain sizes of thin-film polycrystalline semiconductors above the film thickness.[23] For MHP films this has been realized through elevated temperature,[24] high-energy laser pulses[25] or solution-assisted Ostwald ripening.[26,27] However, the poor stability of perovskites[22] poses a fundamental limit to the time and temperature window for post-deposition treatments. Herein, we report a solid-state secondary grain growth method enabling a nearly 10-fold increase of lateral grain size at typical thermal annealing temperature for $MAPbI_3$ perovskites (100°C) within a short period of time (5 minutes). The treatment drives a comprehensive morphological transition towards minimization of surface energy, enabling not only novel photophysical observation of emissive GBs, but also exceptional nanoscale photoconductive uniformity and superior low-light photoresponse, leading to high-performance photodiodes.

Results and discussion

The perovskite ($MAPbI_3$) films are deposited through an established “anti-solvent washing” method followed by thermal annealing.[28] Post-deposition treatment of the $MAPbI_3$ films was carried out in an aerosol-assisted chemical vapor deposition setup,[29] by passing through aerosolized dimethylformamide (DMF) containing methylammonium chloride (MACl, 0.1 mol L^{-1}) carried by continuous nitrogen flow over the film heated at 100°C. The laminar flow of aerosol vaporizes near the film surface and the vapor ingresses into the film. **Figures 1a - 1c** show the scanning electron microscopic (SEM) images of the $MAPbI_3$ films before and after the treatment. The as-deposited $MAPbI_3$ film comprises small grains (Figure 1a), whilst after 5 minutes of treatment closely packed, monolithic grains are formed (Figure 1b). Over-treatment for 10 minutes results in the grains dewetting from the substrates, which leaves voids in the film (Figure 1c), strongly indicating the grain growth is driven by minimization of surface energy.

In **Figure 1d** we demonstrate the critical role of MACl as an additive in driving exceptional grain growth. Increasing the concentration of MACl in the DMF aerosol consistently increases the average lateral grain size of the $MAPbI_3$ films (**Figure S1**) within the fixed time of 5 minutes. Analogous effect can be seen by incorporating similar AX compounds, where A = MA, formamidine (FA) or Cs and X = I or Br, **Figure 1e** and **Figure S2**. Clearly it is the A cation, instead of the halide, that drives exceptional grain growth, as potassium iodide (KI) shows no such effect since it cannot form a stable 3D ABX_3 (here B = Pb) perovskite. MACl is employed in this study as we observed that its lower mass assists the formation of a consistent laminar aerosol flow, and it remains most stable in the DMF against continuous aerosolization.

The morphological change of $MAPbI_3$ films and mechanism of grain growth are schematically illustrated in **Figure 1f**. Ingression of DMF-MACl vapor is insufficient to fully dissolve the $MAPbI_3$ films, but selectively consumes the smaller grains, allowing mass transfer of material from the smaller grains to the larger ones and eventually leading to an increase of overall grain size as time elapses, a process described by Ostwald ripening theory.[23] Contrary to large perovskite grains grown from solution,[13,26,30] the films remain solid state throughout our treatment (**Figure S3**). The absence of a liquid phase prevents additional perovskite nucleation on the surface, thus the overriding process is the growth of existing grains, leading to minimization of both surface energy and surface crystallographic defects.

Whilst DMF vapor is known to break apart perovskite crystals,[29] the role of MACl, as well as other AX (A = Cs, FA, MA, X = Br, I) additives, is to increase the solvating power of DMF thereby driving continuous dissolution of the smaller grains among the existing perovskite grains. We think this is because ingression of MA^+, Cs^+ or FA^+ can distort the $[PbI_6]^{4-}$ octahedra in the $MAPbI_3$ lattice and therefore facilitates the collapse of the 3D perovskite structures, analogous to the dissolution of $MAPbI_3$ films by MA gas.[31] It is worth noting that the additives are mostly expelled from the film when larger $MAPbI_3$ grains are formed, as we observed negligible band gap change that would be expected from incorporation of FA, Cs , Br or Cl. (**Figure S4**).

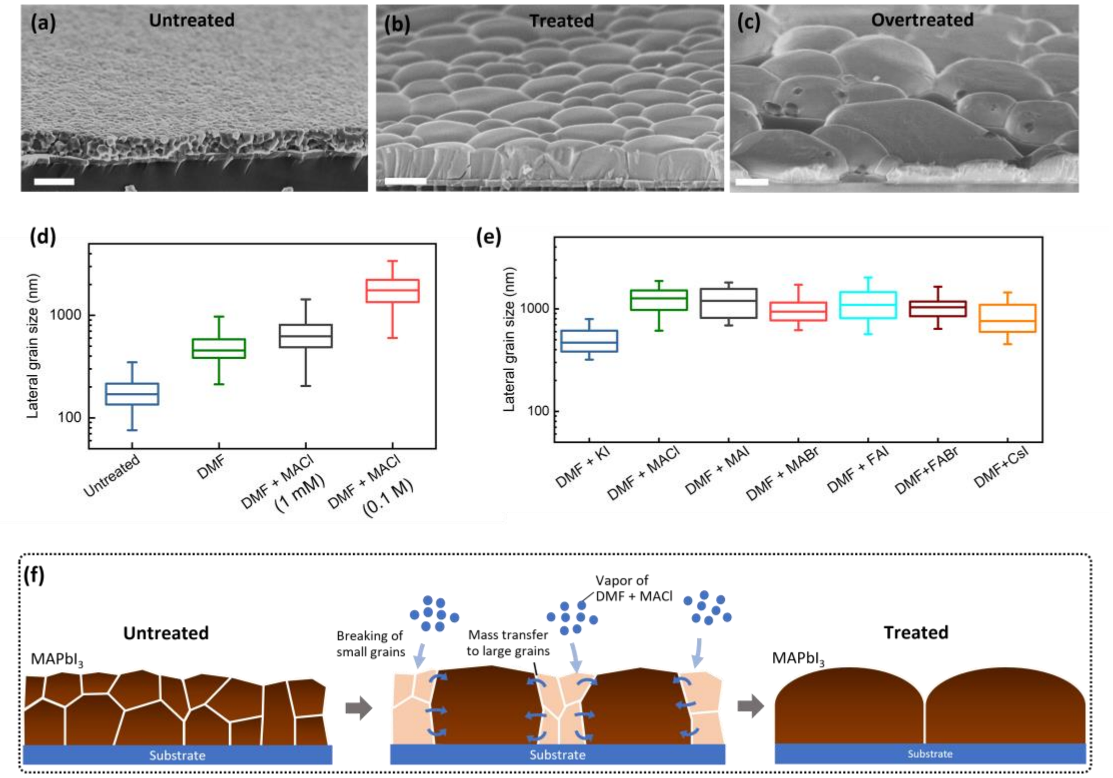

Figure 1. Grain growth of $MAPbI_3$ films induced by treatment with DMF-MACl aerosol. a – c. Tilt-angle cross-section SEM images of untreated $MAPbI_3$ film after antisolvent-assisted spin coating (a), $MAPbI_3$ films treated film for 5 minutes (b) and overtreated for 10 min (c), respectively. Scale bars in all images are 500 nm. **d.** Impact of MACl concentration in DMF on the statistical data of lateral grain size. **e.** Impact of different halide compound additives in DMF (all with concentration of 0.1 M) on the statistical data of lateral grain size. **f.** Schematic drawing of $MAPbI_3$ film morphological transition during MACl treatment and the process of aerosol ingression to the $MAPbI_3$ films, growth of larger $MAPbI_3$ grains at the expense of surrounding smaller grains.

The above results show that by controlling the additives in the aerosol and the time of aerosol ingression, remarkable grain size increase can be achieved whilst the film compactness is maintained. Hereon we focus on the films before (denoted as "untreated") and after 5-minute treatment with 0.1 M MACl in DMF (denoted as "MACl treated"). Surface and cross-sectional SEM images in **Figures 2a - 2d** further highlight the morphological difference. The large number of crystallographic terraces observed on the grains of untreated film (**Figure 2a**), giving a "wrinkled" appearance, indicate the heterogeneous nature of the grain morphology due to rapid crystallization, as such a variety of crystallographic facets are exposed on the surface.[32] The cross-sectional image further elucidates the heterogeneous morphology of the grains (**Figure 2b**). In contrast, the terraces are completely removed from the surface of MACl treated film (**Figure 2c**). The cross-sectional image demonstrates the morphology of the monolithic grains that all have flattened side facets and a smooth convex surface (**Figure 2d**), indicating comprehensive recrystallization at the surfaces and the grain boundaries.

X-ray diffraction (XRD) patterns, **Figure 2e**, shows that the MACl treated film has a large increase of diffraction intensity indicating improved crystallinity, and an approximate 4-fold increase of the relative intensity between the (110) and (310) peak suggesting a strong preferential (110) crystallographic orientation. Closer inspection of the (110) XRD peak, **Figure 2f**, highlights a peak shift to lower 2θ angles after MACl treatment, indicating increased lattice spacing in the out-of-plane directions. This is typically ascribed to relaxation of the residual tensile strains in the in-plane direction,[33] which is achieved through grain growth and morphological transition towards minimized surface energy.

To elucidate the change of charge recombination mechanisms, time-resolved photoluminescence (PL) spectroscopy was measured under varied excitation densities, **Figures 2g – 2h**. The PL decay dynamics of the untreated $MAPbI_3$ film (**Figure 2g**), show typical bi-exponential behavior comprising a fast decay in the first few nanoseconds and a slow decay in tens of nanoseconds.[4] Under the lowest excitation density, 0.028 μJ cm^{-2}, the fast decay quenches over 99.5% of the initial PL, whereas increasing the excitation density consistently reduces the fast-decay component. Such excitation-dependent behavior is assigned to the filling of trap states by photo-generated carriers, and thus the fast-decay component is ascribed to charge trapping.[34,35] In contrast, the fast-decay quenches only around 80% of initial PL in the MACl treated film under 0.028 μJ cm^{-2} (**Figure 2h**). As excitation density increases, the fast-decay magnitude shows much less change whilst the lifetime of slow decay becomes shorter, ascribed to acceleration of band-to-band recombination as the density of photo-generated charge carriers increases. These results show the dominance of trap-assisted recombination in the untreated $MAPbI_3$ film, and that the density of trap states is substantially reduced by the MACl treatment.

Consistent with time-resolved PL data, the steady-state PL spectra show an approximate 12-fold increase of PL intensity by MACl treatment, **Figure 2i**. At the same time, the enhancement of PL emission is accompanied by a change of spectral shape, in that the peak becomes asymmetric and exhibits a "shoulder" on the low-energy side, shown in the inset figure. This indicates that the emissive film exhibits additional radiative recombination pathways with slightly reduced transition energy. We note that we observe a similar increase of grain size and spectral broadening of PL in a $Cs_{0.1}FA_{0.9}Pb(I_{0.95}Br_{0.05})_3$ film after MACl treatment (**Figure S5**), indicating MA is not a critical component for this effect to occur.

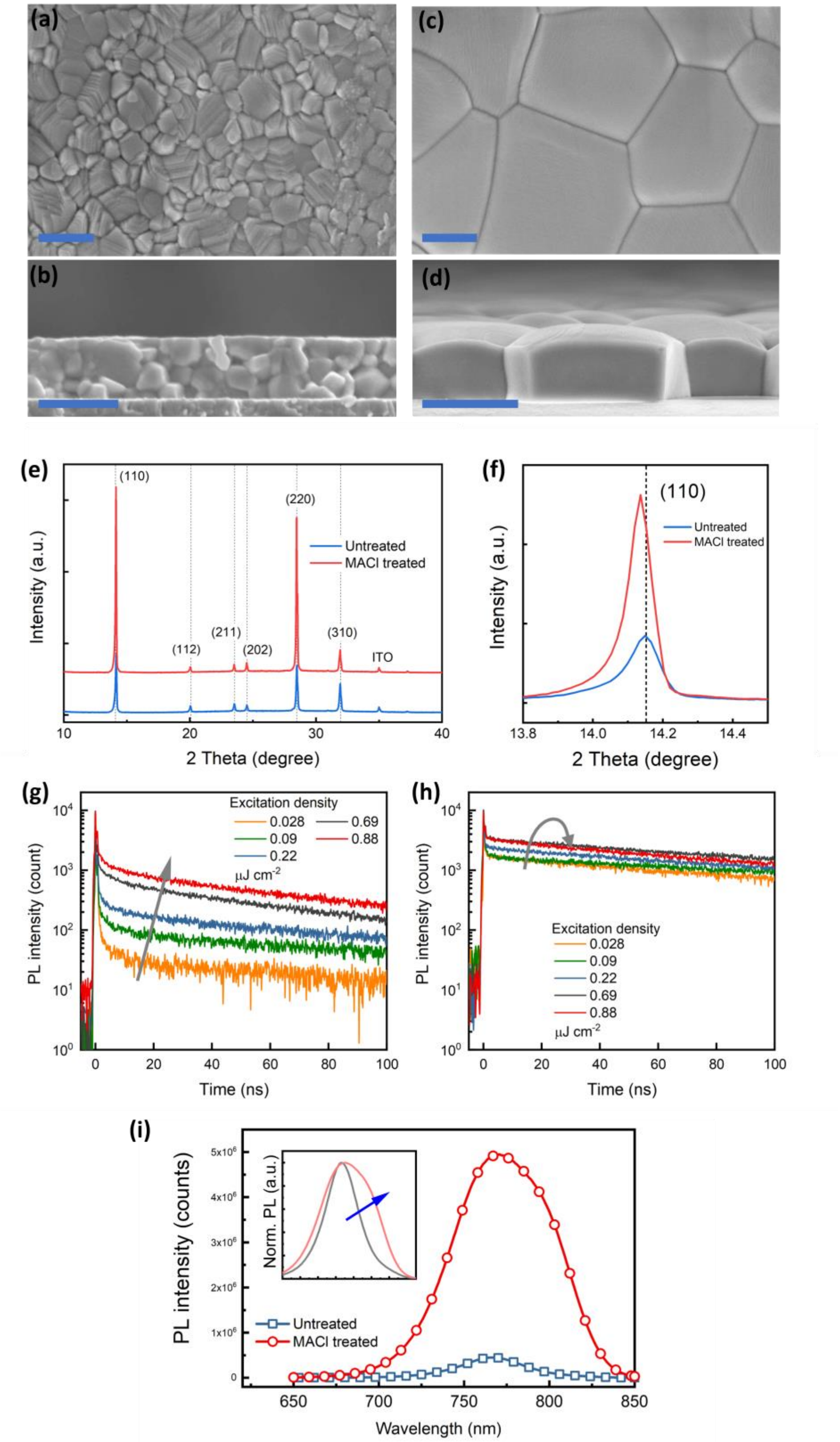

Figure 2. Characterization of MAPbI$_3$ films. a – d. Surface and cross-sectional SEM images of untreated MAPbI$_3$ film (a, b) and MACl treated MAPbI$_3$ film (c, d). Scale bars are 500 nm on all images. **e.** X-ray diffraction patterns of untreated and MACl treated MAPbI$_3$ films. **f.** Zoom-in of the (110) diffraction peak. **g, h.** Time-resolved PL

spectra of untreated $MAPbI_3$ (g) and MACl treated $MAPbI_3$ (h) films, measured with a 435-nm pulsed laser under varied excitation density. **i.** Steady-state PL spectra of $MAPbI_3$ films measured with a 635-nm continuous-wavelength laser with excitation density of 1.5 mW cm^{-2}. The inset figure shows the spectra with normalized PL intensity and the arrow indicates peak broadening of MACl treated film.

To understand the spatial origin of enhanced PL and the spectral "shoulder" we turn to hyperspectral PL maps to probe local spectra. **Figure 3** shows broadband emission maps and of wavelength-specific emission maps at 775 nm and 800 nm from the untreated (**a, b, c**) and MACl treated films (**d, e, f**). The untreated film exhibits local variations of emission intensity in the broadband map (**Figure 3a**) but no clear trend in their spatial distribution is observed in wavelength-specific maps (**Figure 3b** and **3c**), typical to perovskite films prepared with antisolvent washing.[36] In the MACl treated film we are readily able to resolve individual grains, as there is notably intensified PL along the GBs (**Figure 3d**). Looking at the wavelength-specific maps, the brightening of GB is less prominent in the 775 nm map (**Figure 3e**) but is the dominant origin of emission in the 800 nm map (**Figure 3f**), which coincides with the low-energy "shoulder" on in the PL peak. We note that no such GB brightening is exhibited in films treated with DMF-only vapors **(Figure S6**), indicating the critical role that MACl plays in facilitating this behaviour.

To gain further spectral insight, we plot in **Figure 3h** the local spectra at both GB and grain interior from three representative grains (labelled "I" – "III" in Figure 3d), where the spectral difference between GB and grain interior can immediately be seen. All these spectra show a redshift of peak position at the GB regions, with peak area comparable or even greater than grain interiors, highlighting the emissive nature of GBs in MACl treated films. Therefore, we can conclude that the overall spectral asymmetry observed in Figure 2i associated with the emergence a low-energy subpeak stems directly from local brightening at the GBs in MACl treated $MAPbI_3$ film.

The observation of red-shifted PL emission in perovskite films has been ascribed to compression of the perovskite lattice and is usually accompanied by increased charge carrier lifetime,[33,37,38] hereby signalling an improvement of film quality. The emergence of GB emission herein indicates a substantial defect elimination in these regions, whilst the redshift is likely correlated to a relaxation of tensile strains[39] on the side facets of the monolithic grain. The latter is supported by the XRD data where relaxation of in-plane tensile strain leads to increased out-of-plane lattice spacing (Figure 2f). The grain edges show the largest improvement in optoelectronic properties as the GBs have maximum exposure to the DMF-MACl aerosol during the post-treatment. Hence a complete recrystallization preferentially occurs at the edges of existing grains, thereby eliminating the conventionally defective regions. We note that Cl passivation[40] is not likely to play an overriding role in formation of emissive GBs, as Cl-doping of $MAPbI_3$ leads to increase of band gap whereas we observe a redshift. We also exclude the contribution of PL scattering at grain edges to the spectral redshift / broadening by measuring probe-angle-dependent PL spectra, **Figure S7**, in which change in spectral shape by varying the probing angle is negligible compared to the change induced by MACl treatment.

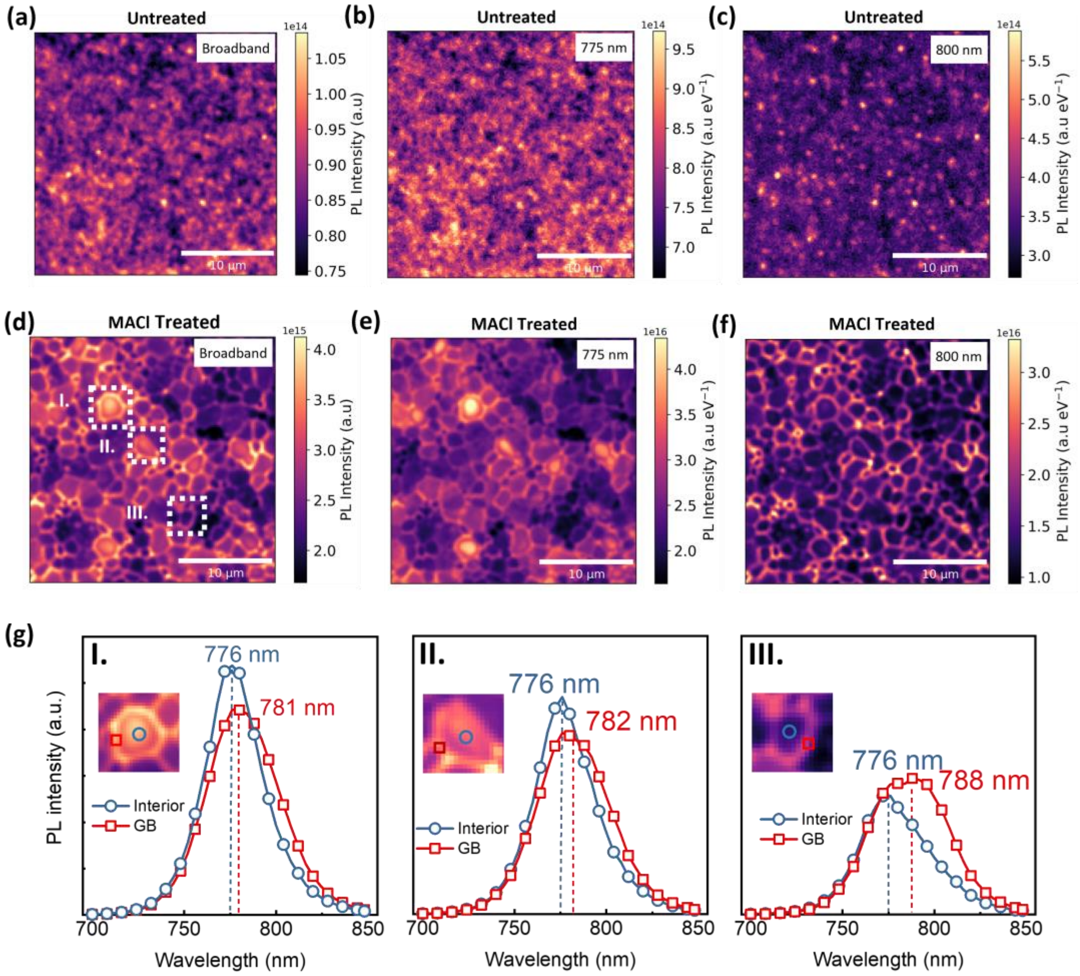

Figure 3. Photoluminescence mapping of MAPbI₃ films. (a) – (f) Hyperspectral PL maps on an untreated MAPbI₃ film (a, b, c) and a MACl treated MAPbI₃ film (d, e, f), probed with broadband detector (a, d) and wavelength-selective detector at 775 nm (b, e) and at 800 nm (c, f), respectively. Maps were taken with 405 nm laser excitation with intensity of 240 mW cm^{-2} in ambient atmosphere. **(g)** Localized PL spectra from three different grain, labelled "I", "II" and "III" in figure d, respectively.

To further examine how the improved quality in the GB regions affects the local optoelectronic properties, we turn to photoconductive atomic force microscopy (pc-AFM) measurements. **Figures 4a - 4h** show the maps for the untreated film (**a** – **d**) and the MACl treated film (**e** - **h**), including height (**a**, **e**), dark current I_{dark} (**b**, **f**), photocurrent I_{ph} (**c**, **g**) and photoresponse (**d**, **h**). Here the photoresponse [nA cm^2 mW^{-1}] is defined as[41]

$$photoresponse = \frac{I_{ph} - I_{dark}}{P_{in}} \quad (1)$$

and is used as an assay of photodetecting properties under certain incident light intensity (P_{in}). We note that direct estimation of the responsivity [A W^{-1}] remains challenging due to difficulty in determining the effective tip-sample emission area and thus the current density.[42] I_{ph} and photoresponse are mapped under varied P_{in} between 0.03 to 160 mW cm^{-2} (**Figures S8 – S9)**. Representative line-scan data taken from an untreated film (line "I") and MACl treated film (lines "II", "III" and "IV") are plotted in **Figure 4i** and **4j**, respectively. Different grains along the line scans are indicated to highlight the intra- and inter-grain variation of these quantities.

The map of I_{dark} highlights a substantial spatial inhomogeneity in untreated $MAPbI_3$ (Figure 4b). The line-scan data (Figure 4i) further elucidates that the variation of I_{dark} is both intra-grain and inter-grain, but in general I_{dark} tends to be greater near the GBs. When illumination of 0.03 mW cm^{-2} is turned on, I_{ph} remains spatially inhomogeneous and does not fully track the distribution of I_{dark} (Figure 4c and 4i). We thus highlight a set of regions in Figure 4b – 4d that exhibit exceptionally high I_{dark} but do not show proportionality of I_{ph} and thereby negligible photoresponse. Importantly, these regions showing negligible photoresponse under this low light levels serve as performance-limiting clusters in the untreated $MAPbI_3$ in terms of photodetection. It can also be observed that these clusters tend to overlap certain crystallographic facets that are particularly defective. Note that these clusters all have stronger photoresponse when light intensity is increased, suggesting that the performance-limiting factor is trap-mediated charge recombination that prevails under weak illumination levels. This in itself is noteworthy, as it allows us to directly visualize trap-rich, performance-limiting regions of the perovskite films. In contrast, the MACl treated film exhibits remarkably improved spatial homogeneity of both I_{dark} and I_{ph}, particularly under weak illumination levels as shown by the maps (Figure 4f and 4g) and line-scan data (Figure 4j). Importantly, the spatial variations of I_{dark} and I_{ph} are minimized both inter-grain and intra-grain, in spite of surface height change being greater than in the untreated film (Figure 4j). Therefore, the GBs in the MACl treated film becomes "invisible" in electrical measurement under dark or weak illumination. The line-scan data also indicates the I_{ph} being much higher than I_{dark} as the illumination is applied, yielding a much stronger photoresponse in the MACl treated film.

We then turn to a quantitative analysis of the photoresponse of what is essentially an ITO/perovskite/Au photoconductor under bias, as indicated in **Figure 4k**. As **Figure 4l** shows, the photoresponse of both films decreases as light intensity increases, but the MACl treated films exhibit substantially enhanced photoresponse and such enhancement is much greater under lower light intensities, showing an increase by a factor of 20 - 40 in the range of 0.03 - 3.2 mW cm^{-2}. We can also observe a much greater variation of both I_{ph} and photoresponse in the untreated film under lower light intensities, which tracks their large spatial inhomogeneity, indicating that the low I_{ph} and poor photoresponse are correlated to the large local variations of these quantities. These results highlight an exceptional improvement in low-light detecting capability using MACl treated films.

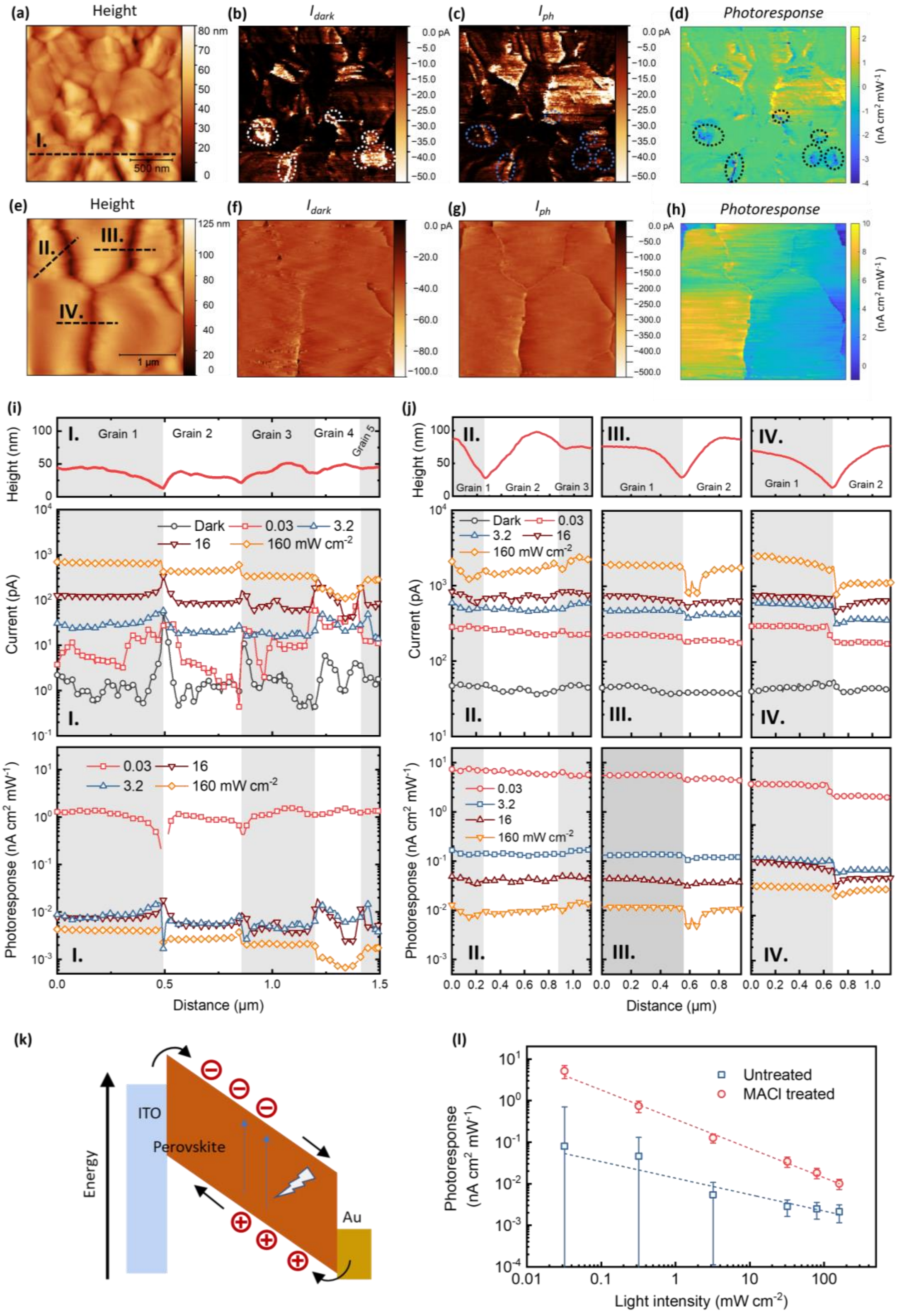

Figure 4. pc-AFM measurement of perovskite films. a – h. pc-AFM maps of untreated MAPbI3 film (a-d) and MACl treated MAPbI3 film (e-h): surface height (a, e), dark current I_{dark} (b, f), and the photocurrent I_{ph} (c, g) and photoresponse (d, h) under

0.03 mW cm^{-2}. Both films are deposited on ITO substrate. All I_{dark} and I_{ph} are measured with applied bias of -1.5 V on ITO. Illumination is provided by a 633-nm laser. **i, j** Line-scan data of height, I_{dark}, I_{ph} and photoresponse taken from untreated film (marked "I.") and from three different positions in MACl treated film (marked "II.", "III." and "IV.", respectively), under varied light intensities from 0.03 to 160 mW cm^{-2}. **k.** Schematic drawing of the energy diagram of ITO/perovskite/Au heterojunction under bias. **l.** Area averaged photoresponse as a function of light intensity. The error bars indicate spatial variation of photoresponse within the measured area.

Finally, to investigate how overcoming local inhomogeneities in $MAPbI_3$ films translates to the performance of full optoelectronic devices, we fabricated and tested perovskite photodiodes (PPD) with the architecture shown in **Figure 5a**. **Figure 5b** plots the current density – voltage (JV) curves in the dark and under illumination (100 mW cm^{-2}). As a key parameter governing the sensitivity of a photodiode, the dark current (J_d) reported for PPDs varies in a wide range depending largely on the engineering of contact layers, and/or defects in the perovskite layer.[43] We herein employ relative thick contact layers that are reported to suppress leakage current and thus reduce J_d (see **Table S1** and **Figure S10**).[44] Even for the PPD with otherwise optimized layer thickness, MACl treatment brings about a remarkable reduction of J_d. At -2 V, for example, the J_d is 2.2×10^{-8} A cm^{-2} for MACl treated PPD, about two orders lower than the J_d of 3.5×10^{-6} A cm^{-2} for the reference PPD. This is among the lowest J_d values reported for a PPD at this bias.[45]

Figure 5c plots the responsivity (R) of the PPDs calculated from the external quantum efficiency (EQE) as an assay of photon-to-electron conversion

$$R = EQE\frac{\lambda q}{hc} \quad (2)$$

where λ is the wavelength of incident light, q the elementary charge, h the Planck's constant, and *c* the speed of light. We can observe a moderate increase of *R* in the MACl treated PPD, but the difference is less significant than that of J_d. To properly calculate the specific detectivity (D*), we measured the noise power spectra for both PPDs, **Figure S11**. The noise floor is reached near 0.3 Hz and the noise current (i_n) at -0.5 V is approximately one order of magnitude lower in the MACl treated PPD, tracking the change of J_d. Here, i_n comprises not only the shot noise from J_d but also the thermal noise from carrier agitation, but it is clear that reduction of J_d can be attributed mostly to the reduction of i_n. Using *R* and i_n we can determine D*, **Figure 5d**, that describes the sensitivity of PPD:

$$D^* = \frac{\sqrt{A\Delta f} \cdot R}{i_n} \quad (3)$$

where *A* is the pixel area, Δf is electrical bandwidth and i_n is noise current. The MACl treated PPD shows higher D^* over the whole spectrum with peak value of 1.24×10^{13} Jones, whilst the peak value of D^* for the reference device is 7.6×10^{12} Jones.

To highlight the improvement of low-light detection, J-V scans are performed under varied light intensities, with J_{ph} at -0.5 V plotted in **Figure 5e**. The MACl treated PPD shows linearity between J_{ph} and light intensity down to approximately 2×10^{-8} W cm^{-2}: two orders of magnitude lower than the value of 10^{-6} W cm^{-2} for the reference PPD. The improvement of low-light detection can be further confirmed by repeated J_{ph} measurement with increasing and decreasing light intensities (**Figure S12**). From these data we can calculate the linear dynamic range (LDR)

$$LDR = 20 \log\left(\frac{J_{max}}{J_{min}}\right) \quad (4)$$

where J_{max} (J_{min}) is the maximum (minimum) value of measured current. The LDR is 93 dB for reference PPD and 126 dB for MACl treated PPD, respectively. We can therefore conclude that the impact of our morphological modification on PPD is manifested by a remarkable reduction of J_d and thus i_n, which enables greater D^* and extended LDR towards lower light levels. These improvements are consistent with the exceptional enhancement of low-light photoresponse observed in pc-AFM measurements on the bare perovskite films.

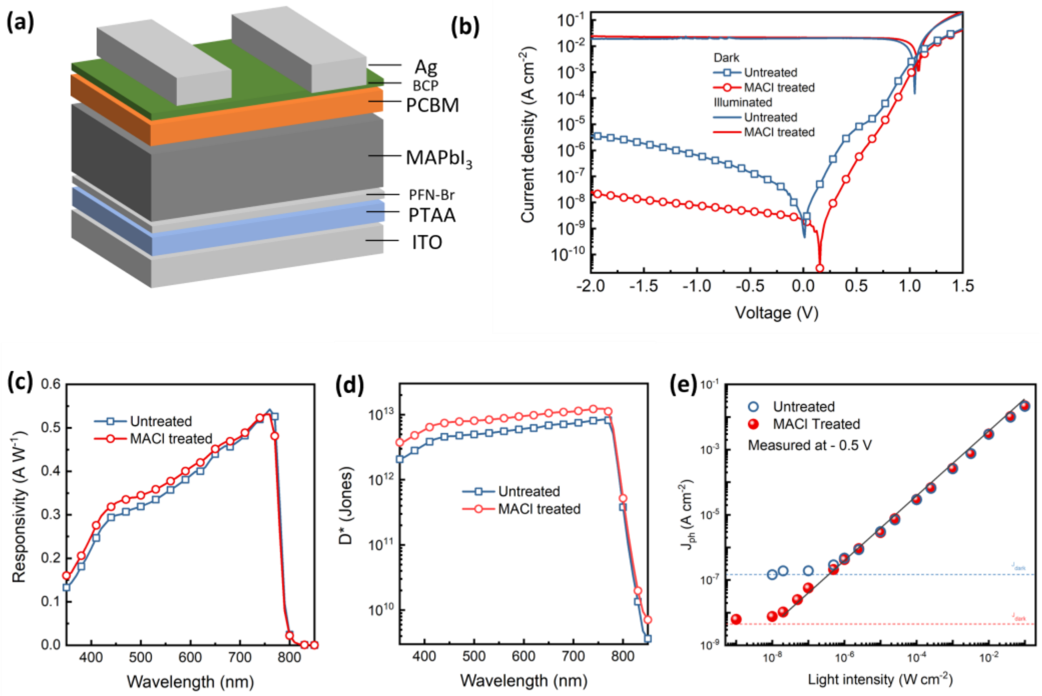

Figure 5. Characterization of perovskite photodiode (PPD). a. Schematic drawing of the architecture of the PPD, where Poly[bis(4-phenyl)(2,4,6-trimethylphenyl)amine (PTAA) is used as electron blacking layer, [6,6]-Phenyl-C61-butyric acid methyl ester (PCBM) as hole blocking layer, Poly(9,9-bis(3'-(N,N-dimethyl)-N-ethylammoinium-propyl-2,7-fluorene)-alt-2,7-(9,9-dioctylfluorene))dibromide (PFN-Br) as the surface modifier of PTAA to reduce its hydrophobicity and bathocuproine (BCP) as interfacial dipole layer for the cathode. **b.** Current density – voltage (J-V) scans of PPD under dark and illumination of 100 mW cm^{-2} provided by an AM1.5G solar simulator. Scan rate is

25 mV s^{-1} in forward direction, from -2 V to 1.5 V. **c.** Responsivity spectra of the PPD, measured under applied bias of -0.5 V. **d.** Specific detectivity (D^*) of the PPD measured at -0.5 V, calculated from detectivity and noise spectra. **e.** Photocurrent measured at -0.5 V bias under varied light intensities, provided by an AM1.5G solar simulator with neutral density filters. The solid line is a linear guideline, and the dashed line indicates the J_{dark} of respective PPDs.

Conclusions

In summary, we have demonstrated the inherent nanoscale inhomogeneity in antisolvent-assisted spin-coated perovskite films, in which the local defective clusters are significant and undermine the overall film quality. These performance-limiting clusters can be effectively eliminated using a vapor-mediated, post-annealing grain growth without the need of passivation agents. The facile treatment leads to remarkable photoluminescence observed at the grain boundaries, and the grain boundaries are almost invisible in local photoconduction measurements, features which are both atypical to polycrystalline thin films. Removing local defective clusters is found to most significantly benefit the low-light photoresponse of perovskite films and perovskite photodiodes, enhancing their low-light detecting capabilities.

In a broader context, our findings highlight an issue that rapid crystallization of perovskite film may have simultaneously created new challenges surrounding material uniformity and optoelectronic quality. The challenges not only undermine the low-light performance of these perovskites but may also limit their performance potential in PV or LED devices. Post-annealing grain growth can be an effective process to resolve this issue towards outstanding material quality and uniformity.

Supporting information available:

Experimental methods, SEM images, PL spectra, photocurrent and photoresponse maps, optimization of layer thickness in PPDs, noise power spectra of the PPDs, cyclic low-light J_{ph} measurements of PPDs.

Acknowledgements

The authors thank the EPSRC Plastic Electronics CDT (EP/L016702/1) for financial support and provision of equipment resource. J.B. and T.D. acknowledge the QMUL-EPSRC Impact Accelerator Account for financial support. T.D. gratefully acknowledges the Stephen and Anna Hui Scholarship (Imperial College London) for financially supporting his doctoral studies. F.R., F.A.C. and S.W. acknowledge funding from the European Union's Horizon 2020 research and Innovation programme under the Marie Skłodowska-Curie grant agreement number 721874 (SPM2.0) and from the UK National Measurement System, via the Department for Business, Energy and Industrial Strategy. K.F. acknowledges a George and Lilian Schiff Studentship, Winton Studentship, the Engineering and Physical Sciences Research Council (EPSRC) studentship, Cambridge Trust Scholarship, and Robert Gardiner Scholarship. S.D.S. acknowledges the Royal Society and Tata Group (UF150033). The work has received funding from the European Research Council under the European Union's Horizon 2020 research and innovation programme (HYPERION - grant agreement no. 756962).

Present address: #T.D.: Institute of Materials for Electronics and Energy Technology (i-MEET), Friedrich-Alexander University Erlangen-Nürnberg, Martensstraße 7, 91058 Erlangen, Germany. Email: tian.du@fau.de.

Reference

(1) Ball, J. M.; Petrozza, A. Defects in Perovskite-Halides and Their Effects in Solar Cells. *Nat. Energy* **2016**, *1* (11), 16149.

(2) Yin, W.-J.; Shi, T.; Yan, Y. Unusual Defect Physics in CH3NH3PbI3 Perovskite Solar Cell Absorber. *Appl. Phys. Lett.* **2014**, *104* (6), 063903/1-063903/4.

(3) Dunlap-Shohl, W. A.; Zhou, Y.; Padture, N. P.; Mitzi, D. B. Synthetic Approaches for Halide Perovskite Thin Films. *Chem. Rev.* **2019**, *119* (5), 3193–3295.

(4) Kim, J.; Godin, R.; Dimitrov, S. D.; Du, T.; Bryant, D.; McLachlan, M. A.; Durrant, J. R. Excitation Density Dependent Photoluminescence Quenching

and Charge Transfer Efficiencies in Hybrid Perovskite/Organic Semiconductor Bilayers. *Adv. Energy Mater.* **2018**, *8* (35), 1802474.

(5) Stranks, S. D.; Burlakov, V. M.; Leijtens, T.; Ball, J. M.; Goriely, A.; Snaith, H. J. Recombination Kinetics in Organic-Inorganic Perovskites: Excitons, Free Charge, and Subgap States. *Phys. Rev. Appl.* **2014**, *2* (3), 1–8.

(6) Deschler, F.; Price, M.; Pathak, S.; Klintberg, L. E.; Jarausch, D. D.; Higler, R.; Hüttner, S.; Leijtens, T.; Stranks, S. D.; Snaith, H. J.; et al. High Photoluminescence Efficiency and Optically Pumped Lasing in Solution-Processed Mixed Halide Perovskite Semiconductors. *J. Phys. Chem. Lett.* **2014**, *5* (8), 1421–1426.

(7) Hutter, E. M.; Hofman, J. J.; Petrus, M. L.; Moes, M.; Abellón, R. D.; Docampo, P.; Savenije, T. J. Charge Transfer from Methylammonium Lead Iodide Perovskite to Organic Transport Materials: Efficiencies, Transfer Rates, and Interfacial Recombination. *Adv. Energy Mater.* **2017**, *7* (13), 1–8.

(8) Senanayak, S. P.; Abdi-Jalebi, M.; Kamboj, V. S.; Carey, R.; Shivanna, R.; Tian, T.; Schweicher, G.; Wang, J.; Giesbrecht, N.; Di Nuzzo, D.; et al. A General Approach for Hysteresis-Free, Operationally Stable Metal Halide Perovskite Field-Effect Transistors. *Sci. Adv.* **2020**, *6* (15), 1–13.

(9) Sutherland, B. R.; Johnston, A. K.; Ip, A. H.; Xu, J.; Adinolfi, V.; Kanjanaboos, P.; Sargent, E. H. Sensitive, Fast, and Stable Perovskite Photodetectors Exploiting Interface Engineering. *ACS Photonics* **2015**, *2* (8),

(10) Lee, H. K. H.; Barbé, J.; Meroni, S. M. P.; Du, T.; Lin, C.; Pockett, A.; Troughton, J.; Jain, S. M.; De Rossi, F.; Baker, J. Outstanding Indoor Performance of Perovskite Photovoltaic Cells–Effect of Device Architectures and Interlayers. *Sol. RRL* **2019**, *3* (1), 1800207.

(11) Jeon, N. J.; Noh, J. H.; Kim, Y. C.; Yang, W. S.; Ryu, S.; Seok, S. Il. Solvent Engineering for High-Performance Inorganic–Organic Hybrid Perovskite Solar Cells. *Nat. Mater.* **2014**, *13* (9), 897–903.

(12) deQuilettes, D. W.; Zhang, W.; Burlakov, V. M.; Graham, D. J.; Leijtens, T.; Osherov, A.; Bulović, V.; Snaith, H. J.; Ginger, D. S.; Stranks, S. D. Photo-Induced Halide Redistribution in Organic–Inorganic Perovskite Films. *Nat. Commun.* **2016**, *7* (5), 11683.

(13) Du, T.; Burgess, C. H.; Lin, C.-T.; Eisner, F.; Kim, J.; Xu, S.; Kang, H.; Durrant, J. R.; McLachlan, M. A. Probing and Controlling Intragrain Crystallinity for Improved Low Temperature–Processed Perovskite Solar Cells. *Adv. Funct. Mater.* **2018**, *28* (51), 1803943. h

(14) Draguta, S.; Thakur, S.; Morozov, Y. V.; Wang, Y.; Manser, J. S.; Kamat, P. V.; Kuno, M. Spatially Non-Uniform Trap State Densities in Solution-Processed Hybrid Perovskite Thin Films. *J. Phys. Chem. Lett.* **2016**, *7* (4), 715–721.

(15) Jones, T. W.; Osherov, A.; Alsari, M.; Sponseller, M.; Duck, B. C.; Jung, Y. K.; Settens, C.; Niroui, F.; Brenes, R.; Stan, C. V.; et al. Lattice Strain Causes Non-Radiative Losses in Halide Perovskites. *Energy Environ. Sci.* **2019**, *12* (2), 596–606.

(16) Dane, W.; Vorpahl, S. M.; Stranks, S. D.; Nagaoka, H.; Eperon, G. E.; Ziffer, M. E.; Snaith, H. J.; Ginger, D. S. Impact of Microstructure on Local Carrier Lifetime in Perovskite Solar Cells. *Science* **2015**, *348* (6235), 683–686.

(17) Jiang, C.; Zhang, P. Crystalline Orientation Dependent Photoresponse and Heterogeneous Behaviors of Grain Boundaries in Perovskite Solar Cells. *J. Appl. Phys.* **2018**, *123* (8), 083105.

(18) Leblebici, S. Y.; Leppert, L.; Li, Y.; Reyes-Lillo, S. E.; Wickenburg, S.; Wong, E.; Lee, J.; Melli, M.; Ziegler, D.; Angell, D. K.; et al. Facet-Dependent Photovoltaic Efficiency Variations in Single Grains of Hybrid Halide Perovskite. *Nat. Energy* **2016**, *1* (8), 1–7.

(19) Du, T.; Burgess, C. H.; Lin, C.-T.; Eisner, F.; Kim, J.; Xu, S.; Kang, H.; Durrant, J. R.; McLachlan, M. A. Probing and Controlling Intragrain Crystallinity for Improved Low Temperature–Processed Perovskite Solar Cells.

Adv. Funct. Mater. **2018**, *28* (51), 1803943.

(20) Li, J. J.; Ma, J. Y.; Ge, Q. Q.; Hu, J. S.; Wang, D.; Wan, L. J. Microscopic Investigation of Grain Boundaries in Organolead Halide Perovskite Solar Cells. *ACS Appl. Mater. Interfaces* **2015**, *7* (51), 28518–28523.

(21) Doherty, T. A. S.; Winchester, A. J.; Macpherson, S.; Johnstone, D. N.; Pareek, V.; Tennyson, E. M.; Kosar, S.; Kosasih, F. U.; Anaya, M.; Abdi-jalebi, M.; et al. Performance-Limiting Nanoscale Trap Clusters at Grain Junctions in Halide Perovskites. *Nature* **2020**, *580* (4), 360–366.

(22) Du, T.; Burgess, C. H.; Kim, J.; Zhang, J.; Durrant, J. R.; McLachlan, M. A. Formation, Location and Beneficial Role of PbI 2 in Lead Halide Perovskite Solar Cells. *Sustain. Energy Fuels* **2017**, *1* (1), 119–126.

(23) Thompson, C. V. Secondary Grain Growth in Thin Films of Semiconductors: Theoretical Aspects. *J. Appl. Phys.* **1985**, *58* (2), 763–772.

(24) Kim, M.; Kim, G. H.; Oh, K. S.; Jo, Y.; Yoon, H.; Kim, K. H.; Lee, H.; Kim, J. Y.; Kim, D. S. High-Temperature-Short-Time Annealing Process for High-Performance Large-Area Perovskite Solar Cells. *ACS Nano* **2017**, *11* (6), 6057–6064.

(25) You, P.; Li, G.; Tang, G.; Cao, J.; Yan, F. Ultrafast Laser-Annealing of Perovskite Films for Efficient Perovskite Solar Cells. *Energy Environ. Sci.* **2020**, *13* (4), 1187–1196.

(26) Yang, M.; Zhang, T.; Schulz, P.; Li, Z.; Li, G.; Kim, D. H.; Guo, N.; Berry, J. J.; Zhu, K.; Zhao, Y. Facile Fabrication of Large-Grain CH3 NH3 PbI3-x Brx Films for High-Efficiency Solar Cells via CH3NH3 Br-Selective Ostwald Ripening. *Nat. Commun.* **2016**, *7* (May), 2–10.

(27) Pham, N. D.; Tiong, V. T.; Yao, D.; Martens, W.; Guerrero, A.; Bisquert, J.; Wang, H. Guanidinium Thiocyanate Selective Ostwald Ripening Induced Large Grain for High Performance Perovskite Solar Cells. *Nano Energy* **2017**, *41* (8), 476–487.

(28) Du, T.; Xu, W.; Daboczi, M.; Kim, J.; Xu, S.; Lin, C. T.; Kang, H.; Lee, K.; Heeney, M. J.; Kim, J. S.; et al. P-Doping of Organic Hole Transport Layers in p-i-n Perovskite Solar Cells: Correlating Open-Circuit Voltage and Photoluminescence Quenching. *J. Mater. Chem. A* **2019**, *7* (32), 18971–18979.

(29) Du, T.; Ratnasingham, S. R.; Kosasih, F. U.; Macdonald, T. J.; Mohan, L.; Augurio, A.; Ahli, H.; Lin, C.-T.; Xu, S.; Xu, W.; et al. Aerosol Assisted Solvent Treatment: A Universal Method for Performance and Stability Enhancements in Perovskite Solar Cells. *Adv. Energy Mater.* **2021**, 2101420.

(30) Cao, X.; Zhi, L.; Li, Y.; Fang, F.; Cui, X.; Ci, L.; Ding, K.; Wei, J. Fabrication of Perovskite Films with Large Columnar Grains via Solvent-Mediated Ostwald Ripening for Efficient Inverted Perovskite Solar Cells. *ACS Appl. Energy Mater.* **2018**, *1* (2), 868–875.

(31) Zhou, Z.; Wang, Z.; Zhou, Y.; Pang, S.; Wang, D.; Xu, H.; Liu, Z.; Padture, N. P.; Cui, G. Methylamine-Gas Induced Defect-Healing Behavior of CH3NH3PbI3 Thin Films for Perovskite Solar Cells. *Angew. Chemie Int. Ed.* **2015**, *54* (33), 9705–9709.

(32) Kutes, Y.; Zhou, Y.; Bosse, J. L.; Steffes, J.; Padture, N. P.; Huey, B. D. Mapping the Photoresponse of CH3NH3PbI3 Hybrid Perovskite Thin Films at the Nanoscale. *Nano Lett.* **2016**, *16* (6), 3434–3441.

(33) Chen, Y.; Lei, Y.; Li, Y.; Yu, Y.; Cai, J.; Chiu, M. H.; Rao, R.; Gu, Y.; Wang, C.; Choi, W.; et al. Strain Engineering and Epitaxial Stabilization of Halide Perovskites. *Nature* **2020**, *577* (7789), 209–215.

(34) Wen, X.; Feng, Y.; Huang, S.; Huang, F.; Cheng, Y.; Green, M.; Ho-baillie, A. Defect Trapping States and Charge Carrier Recombination in Organic – Inorganic Halide. *J. Mater. Chem. C* **2015**, *4*, 793–800.

(35) Yamada, Y.; Endo, M.; Wakamiya, A.; Kanemitsu, Y. Spontaneous Defect Annihilation in CH3NH3PbI3 Thin Films at Room Temperature Revealed by Time-Resolved Photoluminescence Spectroscopy. *J. Phys. Chem. Lett.* **2015**, *6* (3), 482–486.

(36) Andaji-Garmaroudi, Z.; Abdi-Jalebi, M.; Guo, D.; Macpherson, S.; Sadhanala, A.; Tennyson, E. M.; Ruggeri, E.; Anaya, M.; Galkowski, K.; Shivanna, R.; et al. A Highly Emissive Surface Layer in Mixed-Halide Multication Perovskites. *Adv. Mater.* **2019**, *31* (42), 1902374.

(37) Kong, L.; Liua, G.; Gong, J.; Hu, Q.; Schaller, R. D.; Dera, P.; Zhang, D.; Liu, Z.; Yang, W.; Zhu, K.; et al. Simultaneous Band-Gap Narrowing and Carrier-Lifetime Prolongation of Organic-Inorganic Trihalide Perovskites. *Proc. Natl. Acad. Sci.* **2016**, *113* (32), 8910–8915.

(38) Boopathi, K. M.; Martín-García, B.; Ray, A.; Pina, J. M.; Marras, S.; Saidaminov, M. I.; Bonaccorso, F.; Di Stasio, F.; Sargent, E. H.; Manna, L.; et al. Permanent Lattice Compression of Lead-Halide Perovskite for Persistently Enhanced Optoelectronic Properties. *ACS Energy Lett.* **2020**, *5* (2), 642–649.

(39) Zhao, J.; Deng, Y.; Wei, H.; Zheng, X.; Yu, Z.; Shao, Y.; Shield, J. E.; Huang, J. Strained Hybrid Perovskite Thin Films and Their Impact on the Intrinsic Stability of Perovskite Solar Cells. *Sci. Adv.* **2017**, *3* (11), eaao5616.

(40) Jamshaid, A.; Guo, Z.; Hieulle, J.; Stecker, C.; Ohmann, R.; Ono, L. K.; Qiu, L.; Tong, G.; Yin, W.; Qi, Y. Atomic-Scale Insight into the Enhanced Surface Stability of Methylammonium Lead Iodide Perovskite by Controlled Deposition of Lead Chloride. *Energy Environ. Sci.* **2021**, *14* (8), 4541–4554.

(41) Son, Y.; Li, M. Y.; Cheng, C. C.; Wei, K. H.; Liu, P.; Wang, Q. H.; Li, L. J.; Strano, M. S. Observation of Switchable Photoresponse of a Monolayer WSe2-MoS2 Lateral Heterostructure via Photocurrent Spectral Atomic Force Microscopic Imaging. *Nano Lett.* **2016**, *16* (6), 3571–3577.

(42) Frammelsberger, W.; Benstetter, G.; Kiely, J.; Stamp, R. C-AFM-Based Thickness Determination of Thin and Ultra-Thin SiO 2 Films by Use of Different Conductive-Coated Probe Tips. *Appl. Surf. Sci.* **2007**, *253* (7), 3615–3626.

(43) Wang, H.; Kim, D. H. Perovskite-Based Photodetectors: Materials and Devices. *Chem. Soc. Rev.* **2017**, *46* (17), 5204–5236.

(44) Lin, Q.; Armin, A.; Lyons, D. M.; Burn, P. L.; Meredith, P. Low Noise, IR-Blind Organohalide Perovskite Photodiodes for Visible Light Detection and Imaging. *Adv. Mater.* **2015**, *27* (12), 2060–2064.

(45) Fang, Y.; Huang, J. Resolving Weak Light of Sub-Picowatt per Square Centimeter by Hybrid Perovskite Photodetectors Enabled by Noise Reduction. *Adv. Mater.* **2015**, *27* (17), 2804–2810.

ToC graphic